S-Shaped Suppression of the Superconducting Transition Temperature in Cu-Intercalated NbSe$_2$

Huixia Luo,[†,‡] Judyta Strychalska-Nowak,[§] Jun Li,[∥] Jing Tao,[∥] Tomasz Klimczuk,[§] and Robert J. Cava[†]

[†]Department of Chemistry, Princeton University, Princeton, New Jersey 08544, United States

[‡]School of Materials Science and Engineering, Sun Yat-Sen University, No. 135, Xingang Xi Road, Guangzhou 510275, P. R. China

[§]Faculty of Applied Physics and Mathematics, Gdansk University of Technology, Narutowicza 11/12, 80-233 Gdansk, Poland

[∥]Condensed Matter Physics and Materials Science Departments, Brookhaven National Laboratory, Upton, New York 11973, United States

ABSTRACT: 2H-NbSe$_2$ is the prototype and most frequently studied of the well-known transition metal dichalcogenide (TMDC) superconductors. As 2H-NbSe$_2$ is widely acknowledged as a conventional superconductor, its transition temperature to the superconducting state (T_c) is 7.3 K, a T_c that is substantially higher than those seen for the majority of TMDCs, where T_c values between 2 and 4 K are the norm. Here we report the intercalation of Cu into 2H-NbSe$_2$ to make Cu$_x$NbSe$_2$. As is typically found when chemically altering an optimal superconductor, T_c decreases with an increase in x, but the way that T_c is suppressed in this case is unusual: an S-shaped character is observed, with an inflection point near $x = 0.03$ and, at higher x values, a leveling off of the T_c near 3 K, down to the usual value for a layered TMDC. Electronic characterization reveals corresponding S-like behavior for many of the parameters of the materials that influence T_c. To illustrate its character, the superconducting phase diagram for Cu$_x$NbSe$_2$ is contrasted with those of Fe$_x$NbSe$_2$ and NbSe$_{2-x}$S$_x$.
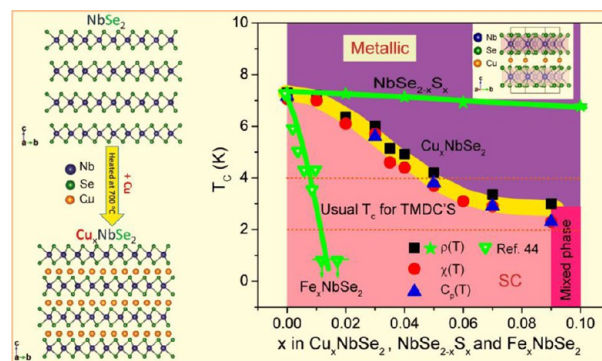
■ INTRODUCTION

Transition metal dichalcogenides (TMDCs) have been studied for decades because of the rich electronic properties that arise because of their low structural dimensionality. These systems share the MX$_2$ formula, where M is a transition metal (M = Ti, Zr, Hf, V, Nb, Ta, Mo, W, or Re) and X is a chalcogen (X = S, Se, or Te);[1–4] the structures are made from stacking X−M−X layers in repeating patterns, with van der Waals (VdW) bonding between the layers. 2H-NbSe$_2$ was one of the earliest layered TMDC materials known to superconduct, with a critical temperature (T_c) of ∼7.3 K. This T_c is significantly higher than those encountered for the many other known TMDC superconductors, for which T_c is commonly in the range of 2−4 K. 2H-NbSe$_2$ also hosts a quasi-two-dimensional incommensurate charge density wave (ICDW) with a T_{CDW} of ∼33 K.[5] It is the most studied of the layered transition metal dichalcogenide superconductors, with almost countless experimental and theoretical papers focusing on its behavior over the past 50 years (see, e.g., refs 6–14). The relation between Fermi surface nesting and its superconductivity is still under debate,[12] for example, even though 2H-NbSe$_2$ has been considered a conventional superconductor for decades.[13] In addition, because of new, recently developed concepts, such as d-wave pairing in cuprates[14] and two-gap superconductivity in MgB$_2$,[15–17] there have been more studies of the super-

conducting order parameters of 2H-NbSe$_2$.[18–21] Many recent experiments performed on 2H-NbSe$_2$, including specific heat,[18] thermal conductivity,[19] magnetization,[20] penetration depth,[21] tunneling spectroscopy,[22–24] and angle-resolved photoemission spectroscopy (ARPES) experiments,[25–29] agree that more than one energy scale is important for superconductivity. Evidence of strong gap anisotropy in 2H-NbSe$_2$ thus appears to be well established, but the question of whether this is a result of there being different superconducting gaps on different Fermi surface sheets or whether it originates elsewhere remains under discussion.

Here we report the results of the intercalation of Cu into 2H-NbSe$_2$ to form Cu$_x$NbSe$_2$[30] in the doping range of $0 \leq x \leq 0.09$, where the 2H structure (see Figure 1A) is maintained; above $x = 0.09$, the material is multiphase and deductions about T_c cannot reliably be made. The T_c decreases with an increasing Cu content in Cu$_x$NbSe$_2$, as is commonly found upon introduction of "impurities" into optimal superconductors, but the way that superconductivity is suppressed is unusual. An S-shaped character is observed in T_c versus x, with an inflection point near $x = 0.03$ and a leveling off, at higher values of x, of
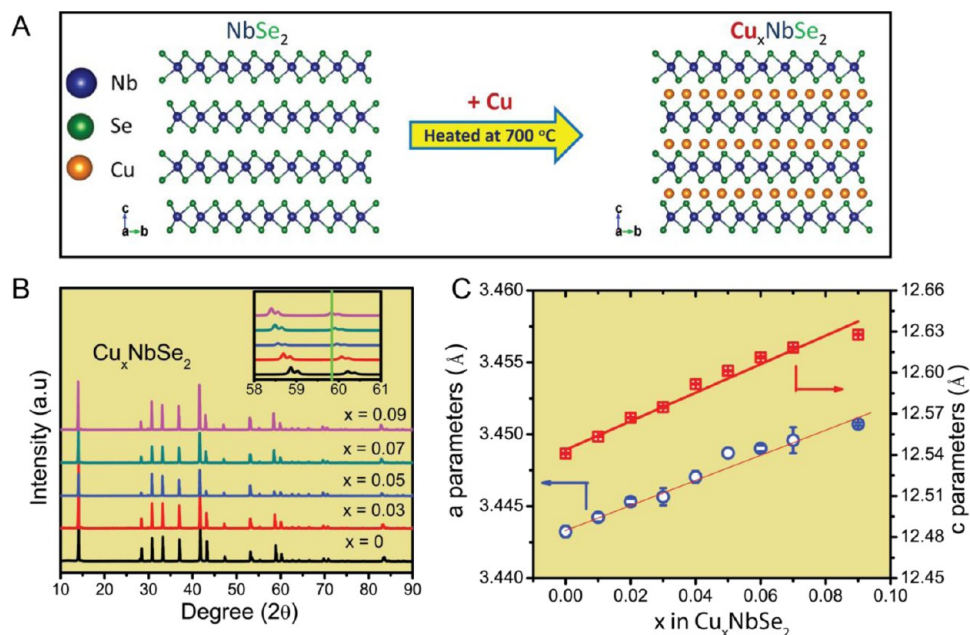
Figure 1. Structural and chemical characterization of Cu_xNbSe_2. (A) Flowchart for Cu intercalation of $2H\text{-}NbSe_2$. The copper-doped materials are synthesized directly from the elements. (B) Powder XRD patterns (Cu $K\alpha$) for the Cu_xNbSe_2 samples studied ($0 \leq x \leq 0.09$). The inset shows a detail of the diffracted angle region where the effect of the increasing cell parameters with an increasing level of Cu intercalation can clearly be seen. (C) Composition dependence of the room-temperature lattice parameters for Cu_xNbSe_2 ($0 \leq x \leq 0.09$); standard deviations are shown when they are larger than the plotted points.

the abnormally high 7 K T_c in the pure phase to a T_c value near 3 K, back down to where it is commonly observed for a layered TMDC. The materials are characterized through measurements of their resistivities, critical fields, magnetic susceptibilities, and heat capacities, which reveal a corresponding S-shaped behavior in the electronic properties of the system, most notably the electronic contribution to the specific heat and the electron–phonon coupling parameter. CDWs compete with superconductivity for stability at low temperatures in the layered TMDCs, and thus the effect of Cu intercalation on the CDW is of interest for obtaining a fuller picture of the electronic system. Our temperature-dependent electron diffraction study reveals a minor change in the **q** vector of the CDW upon Cu intercalation, degradation but not destruction of the coherence of the CDW, especially in the direction perpendicular to the layers, and also the extension of CDW fluctuations, evidenced by diffuse scattering, to room temperature. Comparison of the superconducting phase diagram for Cu_xNbSe_2 to those for the other doped $2H\text{-}NbSe_2$ materials, Fe_xNbSe_2 and $NbSe_{2-x}S_x$, illustrates its unusual character.

■ EXPERIMENTAL SECTION

Polycrystalline samples of Cu_xNbSe_2 were synthesized in two steps by solid state reaction. First, the mixtures of high-purity, cleaned fine powders of Cu (99.9%), Nb (99.9%), and Se (99.999%) in the appropriate stoichiometric ratios were heated in sealed evacuated silica glass tubes at a rate of 1 °C/min to 700 °C and held there for 120 h. Subsequently, the as-prepared powders were reground, repelletized, and sintered again, by being heated at a rate of 3 °C/min to 700 °C and held there for 48 h. The $NbSe_{2-x}S_x$ samples were prepared in the same way. The identity and phase purity of the samples were determined by powder X-ray diffraction (PXRD) using a Bruker D8 Advance ECO instrument with Cu $K\alpha$ radiation and a LYNXEYE-XE detector. To determine the unit cell parameters, profile fits were performed on the powder diffraction data through the use of the

FULLPROF diffraction suite using Thompson−Cox−Hastings pseudo-Voigt peak shapes.[31]

Measurements of the temperature-dependent electrical resistivity (four-contact method), specific heat, and magnetic susceptibility of the materials were performed in a DynaCool Quantum Design Physical Property Measurement System (PPMS). There was no indication of air sensitivity of the materials during the study. T_c values determined from susceptibility data were estimated conservatively. T_c was taken as the intersection of the extrapolations of the steepest slope of the susceptibility in the superconducting transition region and the normal state susceptibility; for resistivities, the midpoint of the resistivity $\rho(T)$ transitions was taken, and for the specific heat data, the critical temperatures obtained from the equal area construction method were employed.

The temperature-dependent electron diffraction experiments were performed on a JEOL 2100F transmission electron microscope equipped with a Gatan liquid helium sample stage. Coherent electron diffraction patterns were recorded with a CCD camera and obtained from the same area in a single-crystal domain for each sample throughout the thermal process. For each sample, electron diffraction patterns acquired from several single-crystal domains were all consistent, with typical results shown here.

■ RESULTS AND DISCUSSION

Panels B and C of Figure 1 show the powder X-ray diffraction patterns and unit cell parameters for Cu_xNbSe_2 ($0 \leq x \leq 0.09$), respectively. The results show that a single phase solid solution is indeed formed. The solubility limit for intercalated Cu in $2H\text{-}NbSe_2$ is $x = 0.09$. At higher Cu contents, the cubic Cu_3NbSe_4 phase is found as an impurity. Within the solid solution, unit cell parameters a and c both increase linearly with an increase in Cu content, in a Vegard's law type behavior: a increases linearly from 3.4432(4) Å ($x = 0$) to 3.4507(1) Å ($x = 0.09$), and c increases linearly from 12.5409(5) Å ($x = 0$) to 12.6277(4) Å ($x = 0.09$). The increase in c with an increase in Cu content is a signature that is characteristic of 3d metal intercalation in TMDCs.[32] The detailed changes in the crystallographic cell in
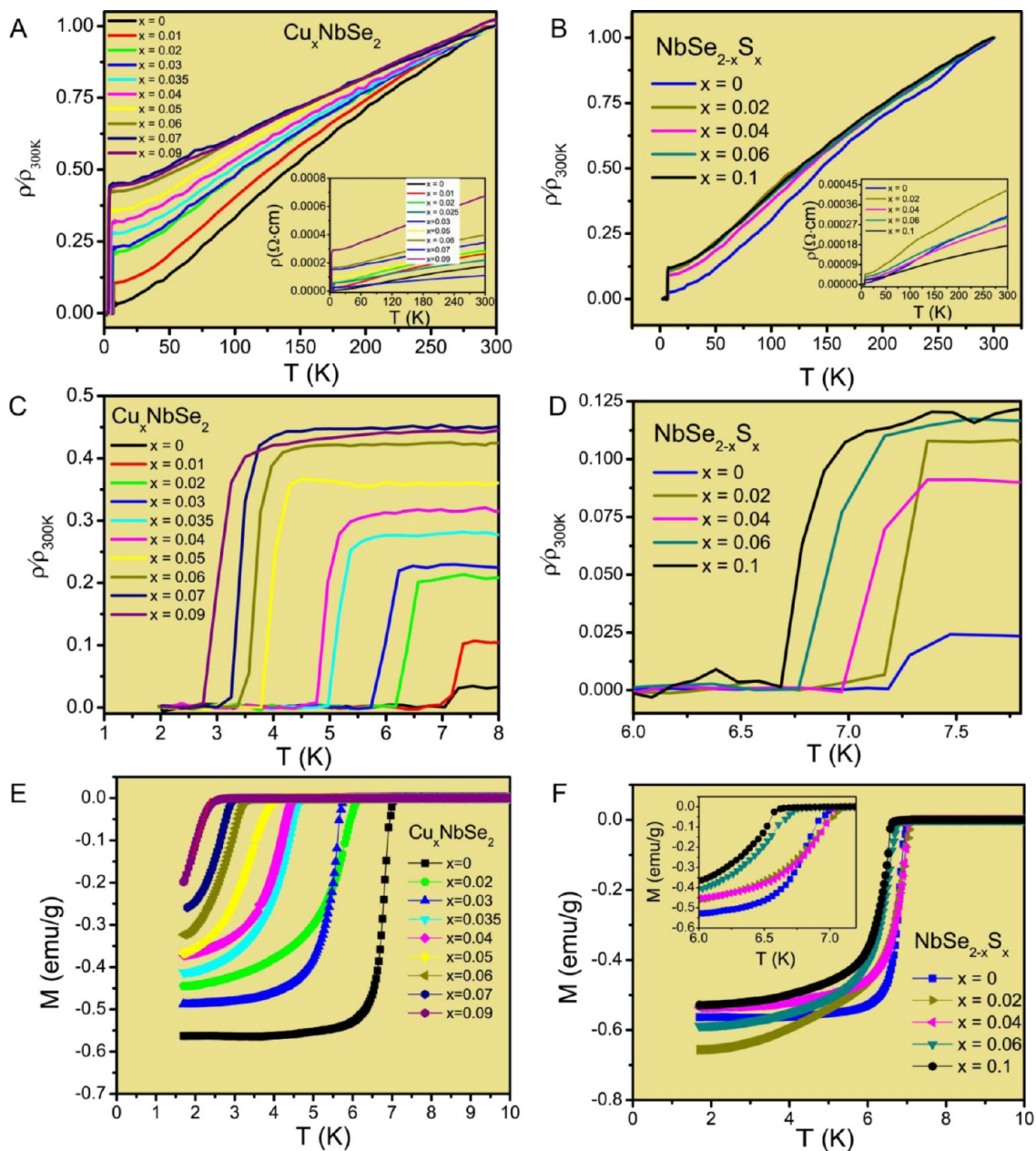
Figure 2. Transport characterization of the normal states and superconducting transitions for (A) Cu_xNbSe_2 and (B) $NbSe_{2-x}S_x$. Temperature dependence of the resistivity ratio $(\rho/\rho_{300\,K})$ for polycrystalline Cu_xNbSe_2 $(0 \leq x \leq 0.09)$ and $NbSe_{2-x}S_x$ $(0 \leq x \leq 0.1)$. (C and D) Enlarged temperature region showing the superconducting transitions. (E and F) Magnetic susceptibilities of Cu_xNbSe_2 $(0 \leq x \leq 0.09)$ and $NbSe_{2-x}S_x$ $(0 \leq x \leq 0.1)$ at the superconducting transitions. Applied DC fields are 20 Oe.

the $NbSe_{2-x}S_x$ system are not the subject of this study and are not presented.

We next consider the temperature dependence of the normalized $(\rho/\rho_{300\,K})$ resistivities of both Cu_xNbSe_2 and $NbSe_{2-x}S_x$. Although careful interpretation of resistivities necessitates the use of data obtained on single crystals, consideration of the data on polycrystalline samples can provide some basic insights. Panels A and B of Figure 2 thus show the temperature dependence of the normalized electrical resistivities $(\rho/\rho_{300\,K})$ for polycrystalline samples of Cu_xNbSe_2 and $NbSe_{2-x}S_x$, respectively. The samples in both cases show a metallic temperature dependence $(d\rho/dT > 0)$ in the temperature region of 8−300 K. However, the relative resistances of the Cu_xNbSe_2 samples decrease substantially less with temperature than those of $NbSe_{2-x}S_x$; the residual

resistivity ratios $[(\text{resistivity at 300 K})/(\text{resistivity just above } T_c)]$ for the polycrystalline samples are, for example, ∼29 for $NbSe_2$, ∼9 for $NbSe_{1.9}S_{0.1}$, and ∼2 for $Cu_{0.09}NbSe_2$. The factor of 15 difference between $NbSe_2$ and $Cu_{0.09}NbSe_2$ suggests that Cu may be an electronically disruptive dopant in $NbSe_2$. At low temperatures (see Figure 2C,D), a clear, sharp drop in $\rho(T)$ is observed in all the Cu_xNbSe_2 and $NbSe_{2-x}S_x$ samples, signifying the onset of superconductivity at low temperatures. T_c decreases with a higher doping content in both cases. This trend is also clearly seen in the susceptibility data (Figure 2E,F); the onset of the negative magnetic susceptibility signaling of the superconducting state shifts systematically to lower temperatures with an increase in x for both Cu_xNbSe_2 and $NbSe_{2-x}S_x$.
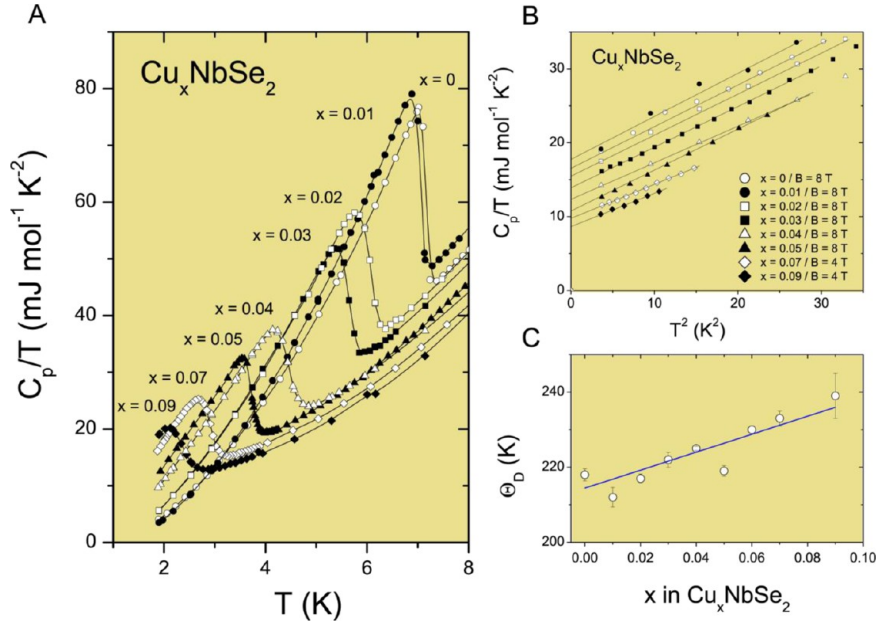
Figure 3. Heat capacity characterization of Cu$_x$NbSe$_2$. (A) Heat capacities through the superconducting transitions without an applied magnetic field for different compositions in Cu$_x$NbSe$_2$. (B) Heat capacities for Cu$_x$NbSe$_2$ for different values of x at an applied magnetic field sufficiently high to fully suppress the superconductivity. Data were used to determine the electronic contribution to the specific heat and the Debye temperatures. (C) Debye temperature of Cu$_x$NbSe$_2$ for different values of x obtained from fits to data in panel B.

Table 1. Characterization of the Superconductivity in the Cu$_x$NbSe$_2$ Family

x in Cu$_x$NbSe$_2$	0	0.01	0.02	0.03	0.035	0.04	0.05	0.06	0.07	0.09
T_c (K)	7.16	7.05	6.04	5.6	5.2	4.46	3.8	3.18	2.9	2.3
γ (mJ mol^{-1} K^{-2})	17.4(20)	17.37(30)	15.58(17)	14.1(1)	–	12.11(10)	10.5(1)	10.4(1)	9.7(1)	8.8(1)
β (mJ mol^{-1} K^{-4})	0.56	0.61	0.56	0.53	–	0.52	0.56	0.49	0.47	0.44
Θ_D (K)	218(16)	212(26)	217(12)	222(20)	–	225(06)	219(14)	230(10)	233(20)	239(60)
$\Delta C/\gamma T_c$	2.04	2.15	1.94	1.96	–	1.81	1.79	1.57	1.68	1.62
λ_{ep}	0.81	0.82	0.76	0.73	–	0.67	0.65	0.60	0.59	0.55
$N(E_F)$ [states eV^{-1} (formula unit)$^{-1}$]	4.08	4.17	3.76	3.45	–	3.07	2.71	2.82	2.60	2.39
$-dH_{c2}/dT$ (T/K)	1.95(4)	2.39(4)	2.29(4)	2.15(15)	2.01(3)	2.25(2)	1.45(4)	–	1.59(5)	–
$\mu_0 H_{c2}$ (T)	9.7(2)	11.7(2)	9.6(2)	8.3(6)	7.2(1)	7.0(1)	3.8(1)	–	3.2(1)	–
$\mu_0 H^P$ (T)	13.2	13.0	11.2	10.4	9.6	8.3	7.0		5.4	
$\xi_{GL}(0)$ (nm)	5.8	5.3	5.9	6.3	6.7	6.9	9.3	–	10.1	–
$\mu_0 H_{c1}$ (T)	0.0158	0.0111	0.0100	0.0080	0.0065	–	0.0056	–	–	–
$\lambda_{GL}(0)$ (nm)	191	237	248	280	314	–	323			
κ_{GL}	33	44	42	45	47	–	35			
$\mu_0 H_c$ (mT)	209	185	160	133	111	–	78			

More detailed information about the electronic properties and superconductivity of the Cu$_x$NbSe$_2$ solid solution was obtained from specific heat measurements. Figure 3A shows the temperature dependence of the zero-field specific heat, C_p/T versus T, for selected Cu$_x$NbSe$_2$ samples. The figure shows that all the materials display a large specific heat jump at T_c, an indication of bulk superconductivity. The superconducting transition temperatures are in excellent agreement with the T_c values determined from the $\rho(T)$ and $\chi(T)$ measurements. The normal state specific heats at low temperatures in the presence of a magnetic field large enough to suppress the superconductivity obey the relation $C_p = \gamma T + \beta T^3$, where γ and β describe the electronic and phonon contributions to the heat capacity, respectively. By fitting the data obtained in the 4 and 8 T applied fields (Figure 3B), we obtain the electronic specific heat coefficients (γ) and phonon specific heat coefficients (β). The normalized specific heat jump values ($\Delta C/\gamma T_c$) thus

obtained from the data in panels A and B of Figure 3 range from 2.04 for 2H-NbSe$_2$ to 1.68 for Cu$_{0.07}$NbSe$_2$. These are all higher than the Bardeen−Cooper−Schrieffer (BCS) weak-coupling limit value (1.43) and clearly decrease with an increase in x. Using the fitted values of β, we estimate the Debye temperatures by the relation $\theta_D = (12\pi \times 4nR/5\beta)^{1/3}$, where n is the number of atoms per formula unit and R is the gas constant. The results (Figure 3C) show that the Debye temperatures increase modestly with increasing Cu content in Cu$_x$NbSe$_2$ as the lattice becomes stiffer when some of the Se−Se VdW bonds are replaced by Se−Cu−Se bonds. These data are summarized in Table 1.

The dependence on x of the superconducting transition temperature and important electronic parameters for Cu$_x$NbSe$_2$ determined from the specific heat data are summarized in Figure 4. Using the Debye temperature (θ_D) and the critical temperature (T_c) and assuming that the electron−phonon
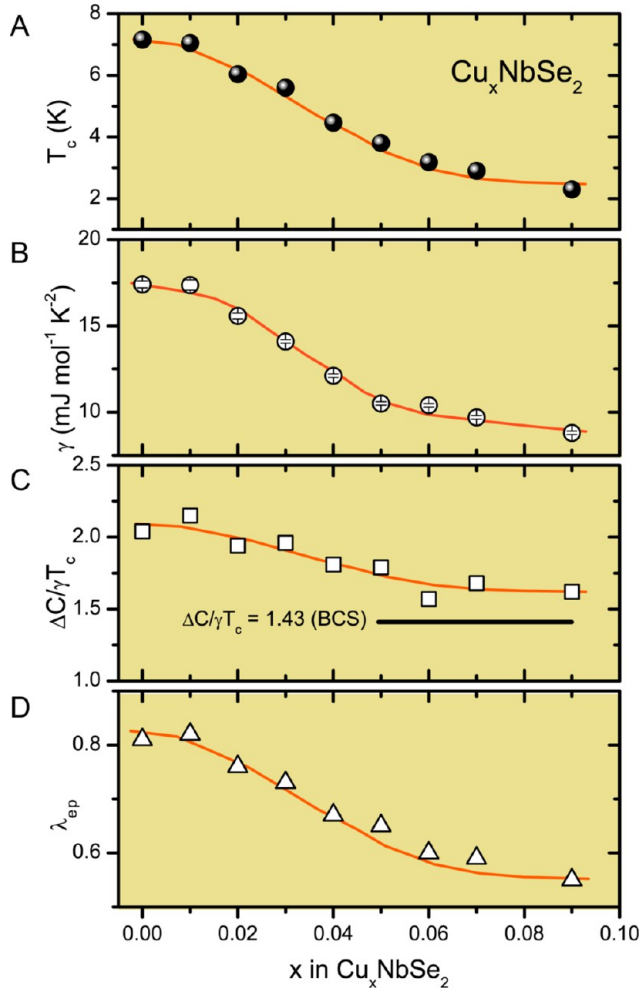
Figure 4. Superconducting transition temperatures for Cu_xNbSe_2 and the associated electronic characteristics. (A) Superconducting transition temperature (T_c) vs x. (B) Electronic contribution to the specific heat, γ, vs x. (C) $\Delta C/\gamma T_c$ vs x. (D) Electron–phonon coupling constant, λ, vs x in Cu_xNbSe_2. An S-like character is observed for all parameters.

coupling constant (λ_{ep}) can be calculated from the inverted McMillan formula:[33]

$$\lambda_{ep} = \frac{1.04 + \mu^* \ln\left(\frac{\theta_D}{1.45T_C}\right)}{(1 - 0.62\mu^*)\ln\left(\frac{\theta_D}{1.45T_C}\right) - 1.04}$$

The values of λ_{ep} obtained range from 0.81 for $2H$-$NbSe_2$ to 0.55 for $Cu_{0.09}NbSe_2$ (Table 1). These values suggest strong coupling superconductivity. With the Sommerfeld parameter (γ) and the electron–phonon coupling (λ_{ep}), the electron density of states at the Fermi level $[N(E_F)]$ can be calculated from the equation $N(E_F) = \{3/[\pi^2 k_B^2(1 + \lambda_{ep})]\}\gamma$. This yields $N(E_F)$ values that range from 4.08 states eV^{-1} (formula unit)$^{-1}$ for $NbSe_2$ to 2.39 states eV^{-1} (formula unit)$^{-1}$ for $Cu_{0.09}NbSe_2$ (Table 1). The density of electronic states at the Fermi energy therefore clearly decreases when more Cu intercalates into $2H$-$NbSe_2$. It can be seen in Figure 4 that the electronic parameters derived from the specific heat for Cu_xNbSe_2 show an S-shaped character that corresponds to that for the superconducting transition temperatures.

The superconducting transitions for selected Cu_xNbSe_2 samples were further examined through temperature-dependent measurements of the electrical resistivity and magnetization under an applied magnetic field, with the goal of determining the critical fields at 0 K, $\mu_0H_{c1}(0)$, $\mu_0H_{c2}(0)$, and $\mu_0H_c(0)$. First, we consider the resistivity measurements employed to determine $\mu_0H_{c2}(0)$. The $\rho(T,H)$ data obtained for Cu_xNbSe_2 ($x = 0$ or 0.05) are shown as an example in panels A and B of Figure 5. On the basis of the T_c determined resistively under different magnetic fields, the upper critical field values, μ_0H_{c2}, are plotted versus temperature in Figure 5C. A clear linear dependence of μ_0H_{c2} versus T is seen near T_c for all samples: the solid lines through the data show the best linear fits. The initial slopes (dH_{c2}/dT) for Cu_xNbSe_2 are listed in Table 1. From these data, we estimate the zero-temperature upper critical fields (top inset in Figure 5F) to range from 9.96 T for $NbSe_2$ to 3.72 T for $Cu_{0.07}NbSe_2$, using the Werthamer–Helfand–Hohenberg (WHH) expression for the dirty limit superconductivity, $\mu_0H_{c2} = -0.693T_c \ (dH_{c2}/dT_c)$.[33−37] The results are summarized in Table 1; the μ_0H_{c2} for $x = 0.01$ is larger than that for $x = 0$, likely because of vortex pinning, and it then decreases with an increase in x. The Pauli limiting field for Cu_xNbSe_2 was estimated from $\mu_0H^P = 1.86T_c$. The obtained values of μ_0H^P are only slightly larger than the estimated μ_0H_{c2}. Finally, using the equation $\mu_0H_{c2} = \phi_0/(2\pi\xi_{GL}^2)$, where ϕ_0 is the quantum of flux, the Ginzburg–Laudau coherence length $[\xi_{GL}(0)]$ can be estimated to range from ~5.3 nm for $Cu_{0.01}NbSe_2$ to ~10.1 nm for $Cu_{0.07}NbSe_2$ (Table 1).

To determine $\mu_0H_{c1}(0)$, the superconducting transition for selected Cu_xNbSe_2 samples was further examined through temperature-dependent measurements of the magnetization under increasing applied magnetic field $M(H)$. The main panel of Figure 5D shows the data for $Cu_{0.05}NbSe_2$ and how μ_0H_{c1} was determined, as an example. First, to estimate the demagnetization factor (N), low-field magnetization measurements as a function of field $M(H)$ were performed at 1.7, 2, 2.5, 3, and 3.5 K, as shown in the main panel of Figure 5D. At low magnetic fields, the experimental data can be fit with the linear formula $M_{fit} = a + bH$. Assuming that the initial linear response to a magnetic field is perfectly diamagnetic ($dM/dH = -1/4\pi$) for these bulk superconductors, we obtained values of N, the demagnetization factor, of 0.1–0.7 [from $-4\pi\chi_V = 1/(1 - N)$, where $\chi_V = dM/dH$ is actually a fitted slope from the main panel of Figure 5D] that are consistent with the sample shape. The $M(H) - M_{fit}$ data are plotted versus the applied magnetic field (H) in the inset of Figure 5D. $\mu_0H_{c1}^*$ is taken as the field where M deviates by ~2% above the fitted line (M_{fit}), as is the common practice.[38] Taking into account the demagnetization factor (N), we can calculate the lower critical field at temperature T, $\mu_0H_{c1}(T)$, from the formula $\mu_0H_{c1}(T) = \mu_0H_{c1}^*(T)/(1 - N)$.[39,40] Figure 5E presents μ_0H_{c1} as a function of temperature for selected Cu_xNbSe_2 samples. The estimation of $\mu_0H_{c1}(0)$ is then possible by fitting the $\mu_0H_{c1}(T)$ data to the formula $\mu_0H_{c1}(T) = \mu_0H_{c1}(0)[1 - (T/T_c)^2]$, which is represented by the solid lines. The estimated zero-temperature lower critical fields $\mu_0H_{c1}(0)$ (see the bottom of the inset of Figure 5F) for Cu_xNbSe_2 ($x = 0, 0.01, 0.02, 0.03, 0.035,$ and 0.05) range from 0.0158 T for $NbSe_2$ to 0.0056 T for $Cu_{0.05}NbSe_2$. From the relation $\mu_0H_{c1}(0) = (\phi_0/4\pi\lambda^2)$ $\ln(\lambda_{GL}/\xi_{GL})$, we numerically find another important superconducting parameter, the magnetic penetration depth (λ_{GL}). This parameter ranges from 191 nm for $NbSe_2$ to 323 nm for $Cu_{0.05}NbSe_2$. The Ginzburg–Landau parameter $\kappa_{GL} = \lambda_{GL}/\xi_{GL}$
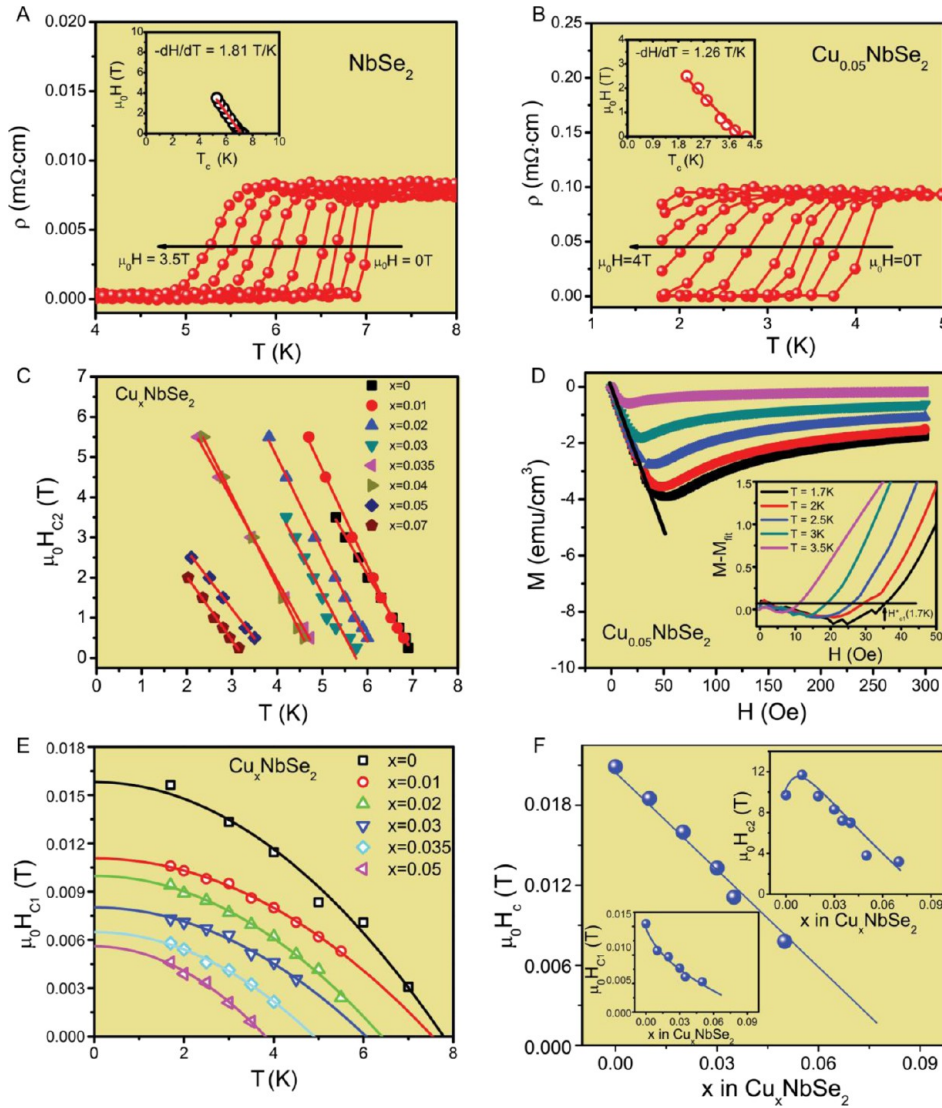
Figure 5. Characterization of the critical fields of Cu_xNbSe_2. (A and B) Low-temperature resistivity at various applied fields for the examples of $NbSe_2$ and $Cu_{0.05}NbSe_2$. (C) Temperature dependence of the upper critical field (μ_0H_{c2}) for Cu_xNbSe_2. (D) Magnetic susceptibility at low applied magnetic fields at various applied temperatures for $Cu_{0.05}NbSe_2$. The inset shows $M - M_{fit}$ vs H. (E) Temperature dependence of the lower critical field (μ_0H_{c1}) for Cu_xNbSe_2. (F) Thermodynamic critical field vs x.

is then calculated and confirms type II superconductivity in Cu_xNbSe_2. The thermodynamic critical field $\mu_0H_c = (\mu_0H_{c1} \times \mu_0H_{c2}/\ln \kappa)^{0.5}$ is shown in Figure 5F. μ_0H_c decreases linearly with increasing Cu content in Cu_xNbSe_2. These parameters are summarized in Table 1.

Figure 6 shows a comparison of the electron diffraction patterns in the basal plane $hk0$ reciprocal lattice for $NbSe_2$ and $Cu_{0.06}NbSe_2$, both at room temperature and at 10 K. The hexagonal symmetry is clearly seen in the intense diffraction spots that arise from the basic structure for both materials at both temperatures. At 10 K, the sharp superlattice diffraction spots because of the CDW (between the intense spots from the basic lattice) are clearly seen for pure $NbSe_2$. Their measured nearly commensurate **q** vector is $0.337a^*$, and they appeared sharply on cooling between 30 and 40 K, consistent with previous observations for 2H-$NbSe_2$.[41,42] The measured widths of the superlattice spots suggest an in-plane coherence of 15–20 nm. Similar, but significantly different in detail, diffraction evidence of CDW formation is also clearly seen in $Cu_{0.06}NbSe_2$. In this case, the spots are less sharp, an indication of a decrease

in coherent diffracting volume, with a measured in-plane coherence of ≤10 nm. The **q** vector of the CDW has changed somewhat, to $0.370a^*$ for $Cu_{0.06}NbSe_2$. Finally, diffuse electron scattering characteristic of CDW formation with short coherence lengths was not clearly visible in undoped $NbSe_2$ above its three-dimensional (3D) CDW transition; i.e., the onset of the 3D CDW was sharp in temperature. In contrast, however, diffuse scattering persists up to room temperature in $Cu_{0.06}NbSe_2$, indicative of short coherence length CDW fluctuations in the Cu-intercalated material up to quite high temperatures. For $Cu_{0.06}NbSe_2$, no sharp transition to 3D ordering is observed; rather, the **q** = $0.37a^*$ diffraction spots visible at 10 K appear to grow approximately continuously out of the diffuse scattering upon cooling. It is natural to ask whether the Cu intercalation disrupts the CDW coherence more in plane than out of plane. This question can be addressed by looking at a larger volume of the reciprocal lattice, shown in Figure 7. Far from the origin of the reciprocal lattice, the curvature of the Ewald sphere allows higher index zones (e.g., $hk1$, $hk2$, etc.) to be sampled. The results for these types
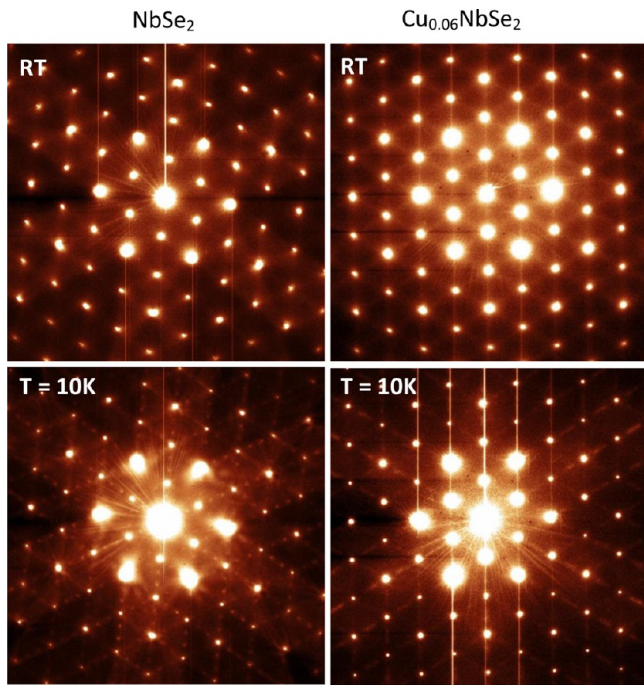
Figure 6. Temperature-dependent electron diffraction characterization of the CDWs in $NbSe_2$ and $Cu_{0.06}NbSe_2$. Typical electron diffraction patterns (along the [001] zone axis, i.e., in the $hk0$ reciprocal lattice plane) obtained from pure $NbSe_2$ (left) and $Cu_{0.06}NbSe_2$ (right). The hexagonal symmetry is clearly seen. For both samples, patterns at room temperature (RT) and low temperatures were obtained from the same area. The vertical streaks are artifacts from the CCD camera. Kikuchi bands are seen in some of the patterns. The CDW in both cases is evidenced by lines of weaker diffraction spots between the main structure spots in the data at 10 K. For the $Cu_{0.06}NbSe_2$ material, diffuse streaks in the diffraction pattern along these lines persist to room temperature.

of reciprocal space probes are shown for diffraction from 2H-$NbSe_2$ and $Cu_{0.06}NbSe_2$ in Figure 7. Again the hexagonal symmetry of the basic structure is clearly seen, as are the superlattice spots due to CDW formation. (The bright rings of spots distant from the origin arise from the intersection of the Ewald sphere with the higher-order basic structure reciprocal lattice planes.) The degradation of the intensity of the superlattice spots on going to higher zones is much larger in the case of pure $NbSe_2$ than it is for $Cu_{0.06}NbSe_2$, and therefore, these diffraction patterns show that the disruption of the CDW is more pronounced perpendicular to the planes than in plane, i.e., that the 3D CDW coherence is more disrupted than the in-plane coherence by Cu intercalation. In both cases, the CDW spots are strong in the $hk0$ zone (near the origin of the reciprocal lattice), consistent with previous studies indicating that the CDW is still present in single-layer $NbSe_2$.[43]

Finally, the superconductivity phase diagram as a function of doping level for 2H-Cu_xNbSe_2 is summarized in Figure 8. For comparison, the superconductivity phase diagram for $NbSe_{2-x}S_x$ ($0 \leq x \leq 0.1$) from the study presented here is included, as is the same information for Fe_xNbSe_2 taken from ref 44. The T_c values extracted from the three kinds of measurements performed here for Cu_xNbSe_2 (resistivity, magnetic susceptibility, and heat capacity) are all consistent; the x dependence of T_c displays an S-like shape in the Cu_xNbSe_2 system, but not in the other systems. The T_c of pure 2H-NbS_2 is 6.5 K,[45] and therefore, the very small change in T_c

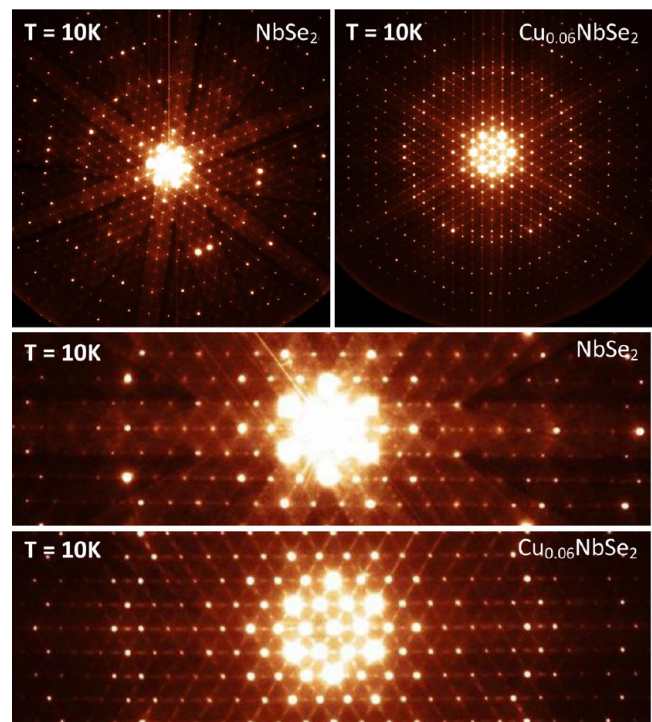**Figure 7.** Electron diffraction patterns at 10 K over a wider volume of reciprocal space in $NbSe_2$ and $Cu_{0.06}NbSe_2$. The intensity distributions of the CDW reflections strongly suggest the following. (1) The atomic displacements associated with the CDW modulation are longitudinal in both cases, and (2) the CDW modulation is relatively weakly correlated between layers (along the c-axis) for both materials. For $Cu_{0.06}NbSe_2$, the correlation of the CDW along the c-axis is weaker, based on the fact that the intensities of the CDW diffuse reflections remain strong close to the $hk1$ Laue zone. Kikuchi bands and the hexagonal symmery of the patterns are clearly seen.
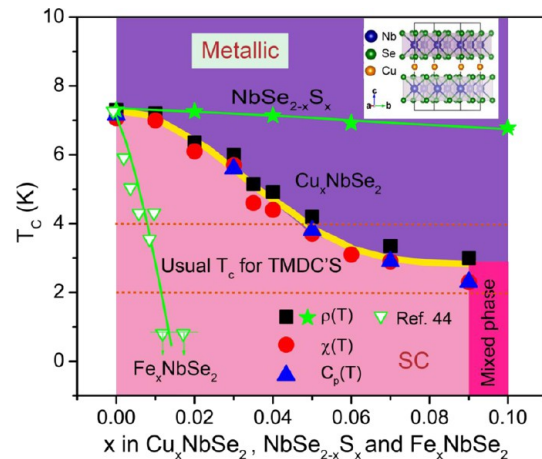

Figure 8. Superconducting phase diagram for 2H-Cu_xNbSe_2 compared to those of 2H-$NbSe_{2-x}S_x$ from the study presented here and 2H-Fe_xNbSe_2 from ref 44. The usual range of T_c values for transition metal dichalcogenides is illustrated by the dashed lines. "SC" and "metallic" label the superconducting and metallic regions for Cu_xNbSe_2, respectively. The labels $\rho(T)$, $\chi(T)$, and $C_p(T)$ are the T_c values determined for the materials in this study from resistivity, magnetic susceptibility, and specific heat characterization, respectively. The limit of the Cu_xNbSe_2 solubility is $x = 0.09$; beyond that x value, the materials contain multiple phases (the solubility extends to at least $x = 0.1$ for $NbSe_{2-x}S_x$.) The top right inset shows a schematic of the crystal structure of Cu_xNbSe_2.

of the sulfur-doped material may not be surprising. (Work on Cu_xNbS_2 similar to that performed in the study presented here may therefore be of interest in the future.) In contrast, intercalated Fe may be considered as a magnetic ion, with the magnetism leading to a very rapid suppression of T_c with an increasing Fe content. Therefore, nonmagnetic chemically different Cu intercalation is naively expected to act somewhere between the Fe- and S-doped extremes, although not with an S-shaped behavior; there are no previously known examples of an S-shaped suppression of T_c by substitution or doping in a single-phase material.

CONCLUSION

Cu_xNbSe_2 ($0 \leq x \leq 0.09$) was prepared by a solid state method. The electronic properties, including resistivity, heat capacity, and critical fields, were studied in detail and indicate that copper doping suppresses the superconductivity in $NbSe_2$ in an unexpected way; the electronic properties and x-dependent electronic phase diagram show that the superconducting transition temperature of Cu-intercalated $NbSe_2$ shows an unusual S-shaped behavior. The underlying reason for this usual S-shape behavior of T_c and the electronic characteristics that give rise to it have not been determined here. However, on the basis of the fact that the T_c is unusually high for pure $NbSe_2$ and then settles to the usual value for TMDCs for Cu_xNbSe_2, it is not unreasonable to speculate that Cu doping destroys the higher-energy paring channel that makes $NbSe_2$ unusual among the layered TMDCs. We speculate that this may be due to either the electron doping of the $NbSe_2$ layer that results in Cu intercalation or the nonmagnetic disorder introduced by the Cu intercalation. The lower T_c cannot, for example, simply be due to a strengthening of the competing CDW state for a non-zero x in Cu_xNbSe_2, because the electron diffraction studies show that such strengthening is clearly not the case. It may, however, be that the Cu intercalation both disrupts the coherence of the CDW and simultaneously suppresses the pairing channel that gives rise to the higher T_c in $NbSe_2$. Future detailed characterization experiments and theoretical treatments will be required to determine whether this speculation is indeed the case.

REFERENCES

(1) Withers, R. L.; Bursill, L. A. The structure of the incommensurate superlattices of 2H-TaSe$_2$. *Philos. Mag. B* **1981**, *43*, 635−672.

(2) Arguello, C. J.; Chockalingam, S. P.; Rosenthal, E. P.; Zhao, L.; Gutíerrez, C.; Kang, J. H.; Chung, W. C.; Fernandes, R. M.; Jia, S.; Millis, A. J.; Cava, R. J.; Pasupathy, A. N. Visualizing the charge density wave transition in 2H-NbSe$_2$ in real space. *Phys. Rev. B: Condens. Matter Mater. Phys.* **2014**, *89*, 235115.

(3) Soumyanarayanan, A.; Yee, M. M.; He, Y.; van Wezel, J.; Rahn, D. J.; Rossnagel, K.; Hudson, E. W.; Norman, M. R.; Hoffman, J. E. Quantum phase transition from triangular to stripe charge order in NbSe$_2$. *Proc. Natl. Acad. Sci. U. S. A.* **2013**, *110*, 1623−1627.

(4) Matthias, B. T.; Geballe, T. H.; Compton, V. B. Superconductivity. *Rev. Mod. Phys.* **1963**, *35*, 1.

(5) Revolinsky, E.; Lautenschlager, E. P.; Armitage, C. H. Layer structure superconductor. *Solid State Commun.* **1963**, *1*, 59−61.

(6) Wilson, J. A.; Di Salvo, F. J.; Mahajan, S. Charge-density waves in metallic, layered, transition-metal dichalcogenides. *Phys. Rev. Lett.* **1974**, *32*, 882.

(7) Boaknin, E.; Tanatar, M. A.; Paglione, J.; Hawthorn, D.; Ronning, F. R.; Hill, W.; Sutherland, M.; Taillefer, L.; Sonier, J.; Hayden, S. M.; Brill, J. W. Heat conduction in the vortex state of NbSe$_2$: evidence for multiband superconductivity. *Phys. Rev. Lett.* **2003**, *90*, 117003.

(8) Suderow, H.; Tissen, V. G.; Brison, J. P.; Martínez, J. L.; Vieira, S. Pressure induced effects on the fermi surface of superconducting 2H-NbSe$_2$. *Phys. Rev. Lett.* **2005**, *95*, 117006.

(9) Du, C. H.; Lin, W. J.; Su, Y.; Tanner, B. K.; Hatton, P. D.; Casa, D.; Keimer, B.; Hill, J. P.; Oglesby, C. S.; Hohl, H. X-ray scattering studies of 2H-NbSe$_2$, a superconductor and charge density wave material, under high external magnetic fields. *J. Phys.: Condens. Matter* **2000**, *12*, 5361−5370.

(10) Xi, X. X.; Zhao, L.; Wang, Z. F.; Berger, H.; Forró, L.; Shan, L. F. J.; Mak, K. F. Strongly enhanced charge-density-wave order in monolayer NbSe$_2$. *Nat. Nanotechnol.* **2015**, *10*, 765−770.

(11) Ménard, G. C.; Guissart, S.; Brun, C.; Pons, S.; Stolyarov, V. S.; Debontridder, F.; Leclerc, M. V.; Janod, E.; Cario, L.; Roditchev, D.; Simon, P.; Cren, T. Coherent long-range magnetic bound states in a superconductor. *Nat. Phys.* **2015**, *11*, 1013−1016.

(12) Kiss, T.; Yokoya, T.; Chainani, A.; Shin, S.; Hanaguri, T.; Nohara, M.; Takagi, H. Hidden Charge-Density-Wave Order in a Low-T$_c$ Superconductor 2H-NbSe$_2$. https://arxiv.org/vc/cond-mat/papers/0310/0310326v1.pdf.

(13) Johannes, M. D.; Mazin, I. I.; Howells, C. A. Fermi-surface nesting and the origin of the charge-density wave in NbSe$_2$. *Phys. Rev. B: Condens. Matter Mater. Phys.* **2006**, *73*, 205102.

(14) Corcoran, R. C.; Meeson, P. J.; Onuki, Y.; Probst, P. A.; Springford, M.; Takita, K.; Harima, H.; Guo, G. Y.; Gyorffy, B. L. Quantum oscillations in the mixed state of the type II superconductor 2H-NbSe$_2$. *J. Phys.: Condens. Matter* **1994**, *6*, 4479−4492.

(15) Tsuei, C. C.; Kirtley, J. R. d-Wave pairing symmetry in cuprate superconductors—fundamental implications and potential applications. *Phys. C* **2002**, *367*, 1−8.

(16) Souma, S.; Machida, Y.; Sato, T.; Takahashi, T.; Matsui, H.; Wang, S. C.; Ding, H.; Kaminski, A.; Campuzano, J. C.; Sasaki, S.; Kadowaki, K. The origin of multiple superconducting gaps in MgB$_2$. *Nature* **2003**, *423*, 65−67.

(17) Örd, T.; Kristoffel, N. Modeling MgB$_2$ two-gap superconductivity. *Phys. C* **2002**, *370*, 17−20.

(18) Kristoffel, N.; Örd, T.; Rägo, K. MgB$_2$ two-gap superconductivity with intra- and interband couplings. *EPL* **2003**, *61*, 109−115.

(19) Huang, C. L.; Lin, J.-Y.; Chang, Y. T.; Sun, C. P.; Shen, H. Y.; Chou, C. C.; Berger, H.; Lee, T. K.; Yang, H. D. Experimental evidence for a two-gap structure of superconducting NbSe$_2$: A specific-heat study in external magnetic fields. *Phys. Rev. B: Condens. Matter Mater. Phys.* **2007**, *76*, 212504.

(20) Boaknin, E.; Tanatar, M. A.; Paglione, J.; Hawthorn, D.; Ronning, F.; Hill, R. W.; Sutherland, M.; Taillefer, L.; Sonier, J.; Hayden, S. M.; Brill, J. W. Heat Conduction in the Vortex State of $NbSe_2$: Evidence for Multiband Superconductivity. *Phys. Rev. Lett.* **2003**, *90*, 117003.

(21) Zehetmayer, M.; Weber, H. W. Experimental evidence for a two-band superconducting state of $NbSe_2$ single crystals. *Phys. Rev. B: Condens. Matter Mater. Phys.* **2010**, *82*, 014524.

(22) Fletcher, J. D.; Carrington, A.; Diener, P.; Rodière, P.; Brison, J. P.; Prozorov, R.; Olheiser, T.; Giannetta, R. W. Penetration Depth Study of Superconducting Gap Structure of $2H-NbSe_2$. *Phys. Rev. Lett.* **2007**, *98*, 057003.

(23) Rodrigo, J. G.; Vieira, S. STM study of multiband superconductivity in $NbSe_2$ using a superconducting tip. *Phys. C* **2004**, *404*, 306−310.

(24) Guillamon, I.; Suderow, H.; Guinea, F.; Vieira, S. Intrinsic atomic-scale modulations of the superconducting gap of $2H-NbSe_2$. *Phys. Rev. B: Condens. Matter Mater. Phys.* **2008**, *77*, 134505.

(25) Noat, Y.; Cren, T.; Debontridder, F.; Roditchev, D.; Sacks, W.; Toulemonde, P.; San Miguel, A. Signatures of multigap superconductivity in tunneling spectroscopy. *Phys. Rev. B: Condens. Matter Mater. Phys.* **2010**, *82*, 014531.

(26) Rahn, D. J.; Hellmann, S.; Kalläne, M.; Sohrt, C.; Kim, T. K.; Kipp, L.; Rossnagel, K. Gaps and kinks in the electronic structure of the superconductor $2H-NbSe_2$ from angle-resolved photoemission at 1 K. *Phys. Rev. B: Condens. Matter Mater. Phys.* **2012**, *85*, 224532.

(27) Yokoya, T.; Kiss, T.; Chainani, A.; Shin, S.; Nohara, M.; Takagi, H. Fermi Surface Sheet-Dependent Superconductivity in $2H-NbSe_2$. *Science* **2001**, *294*, 2518−2520.

(28) Tonjes, W. C.; Greanya, V. A.; Liu, R.; Olson, C. G.; Molinié, P. Charge-density-wave mechanism in the $2H-NbSe_2$ family: Angle-resolved photoemission studies. *Phys. Rev. B: Condens. Matter Mater. Phys.* **2001**, *63*, 235101.

(29) Xi, X. X.; Wang, Z. F.; Zhao, W. W.; Park, J. H.; Law, K. T.; Berger, H.; Forró, L. J.; Shan, J.; Mak, K. F. Ising pairing in superconducting $NbSe_2$ atomic layers. *Nat. Phys.* **2016**, *12*, 139−144.

(30) Koh, Y. Y.; Kim, Y. K.; Jung, W. S.; Han, G. R.; Park, S. R.; Leem, C. S.; Kim, C.; Song, D. J.; Kyung, W. S.; Choi, H. Y.; Yang, L. X.; He, C.; Chen, F.; Feng, D. L.; Kim, C. Photoemission studies of Cu intercalated $NbSe_2$. *J. Phys. Chem. Solids* **2011**, *72*, 565−567.

(31) Rodríguez-Carvajal, J. Recent developments of the program FULLPROF. *Commission on Powder Diffraction* **2001**, *26*, 12−19.

(32) Voorhoeve, J. M.; van den Berg, N.; Robbins, M. Intercalation of the Niobium-Diselenide Layer Structure by First-Row Transition Metals. *J. Solid State Chem.* **1970**, *1*, 134−137.

(33) McMillan, W. L. Transition temperature of strong-coupled superconductors. *Phys. Rev.* **1968**, *167*, 331.

(34) Wilson, J. A.; Barker, A. S.; Di Salvo, F. J.; Ditzenberger, J. A. Ditzenberger, Infrared properties of the semimetal $TiSe_2$. *Phys. Rev. B: Condens. Matter Mater. Phys.* **1978**, *18*, 2866−2875.

(35) Kohn, W. Excitonic Phases. *Phys. Rev. Lett.* **1967**, *19*, 439−442.

(36) Werthamer, N. R.; Helfand, E.; Hohenberg, P. C. Temperature and Purity Dependence of the Superconducting Critical Field, H_{c2}. III. Electron Spin and Spin-Orbit Effects. *Phys. Rev.* **1966**, *147*, 295.

(37) Kresin, V. Z.; Wolf, S. A. *Fundamentals of superconductivity*; Plenum Press: New York, 1990; pp 150−153.

(38) Luo, H. X.; Xie, W. W.; Tao, J.; Pletikosic, I.; Valla, T. G.; Sahasrabudhe, S.; Osterhoudt, G.; Sutton, E.; Burch, K. S.; Seibel, E. M.; Krizan, J. W.; Zhu, Y. M.; Cava, R. J. Differences in chemical doping matter - Superconductivity in $Ti_{1-x}Ta_xSe_2$ but not in $Ti_{1-x}Nb_xSe_2$. *Chem. Mater.* **2016**, *28*, 1927−1935.

(39) Winiarski, M. J.; Wiendlocha, B.; Gołąb, S.; Kushwaha, S. K.; Wiśniewski, P.; Kaczorowski, D.; Thompson, J. D.; Cava, R. J.; Klimczuk, T. Superconductivity in $CaBi_2$. *Phys. Chem. Chem. Phys.* **2016**, *18*, 21737−21745.

(40) Yadav, C. S.; Paulose, P. L. Upper critical field, lower critical field and critical current density of $FeTe_{0.60}Se_{0.40}$ single crystal. *New J. Phys.* **2009**, *11*, 103046.

(41) Kiss, T.; Yokoya, T.; Chainani, A.; Shin, S.; Hanaguri, T.; Nohara, M.; Takagi, H. Charge-order-maximized momentum dependent superconductivity. *Nat. Phys.* **2007**, *3*, 720−725.

(42) Naik, I.; Rastogi, A. K. Charge density wave and superconductivity in 2H- and $4H-NbSe_2$: A revisit. *Pramana* **2011**, *76*, 957−963.

(43) Ugeda, M. M.; Bradley, A. J.; Zhang, Y.; Onishi, S.; Chen, Y.; Ruan, W.; Ojeda-Aristizabal, C.; Ryu, H.; Edmonds, M. T.; Tsai, H. Z.; Riss, A.; Mo, S. K.; Lee, D. H.; Zettl, A.; Hussain, Z.; Shen, Z. X.; Crommie, M. F. Characterization of collective ground states in single-layer $NbSe_2$. *Nat. Phys.* **2016**, *12*, 92−97.

(44) Hauser, J. J.; Robbins, M.; DiSalvo, F. J. Effect of 3d Impurities on the Superconducting Transition Temperature of the Layered Compound $NbSe_2$. *Phys. Rev. B* **1973**, *8*, 1038−1042.

(45) Fisher, W. G.; Sienko, M. J. Stoichiometry, structure, and physical properties of niobium disulfide. *Inorg. Chem.* **1980**, *19*, 39−43.